



Nanopillar quantum well lasers directly grown on silicon and emitting at silicon-transparent wavelengths

FANGLU LU,^{1,†} INDRASEN BHATTACHARYA,^{2,†} HAO SUN,³ THAI-TRUONG D. TRAN,² KAR WEI NG,¹ GILLIARD N. MALHEIROS-SILVEIRA,¹  AND CONNIE CHANG-HASNAIN^{1,2,4,*}

¹Department of Electrical Engineering and Computer Sciences, University of California at Berkeley, Berkeley, California 94720, USA

²Applied Science and Technology Group, University of California at Berkeley, Berkeley, California 94720, USA

³Department of Electronic Engineering, Tsinghua University, Beijing 100084, China

⁴Tsinghua Berkeley Shenzhen Institute, University of California at Berkeley, Berkeley, California 94720, USA

*Corresponding author: cch@berkeley.edu

Received 14 February 2017; revised 27 April 2017; accepted 28 April 2017 (Doc. ID 286626); published 23 June 2017

Future expansion of computing capabilities relies on a reduction of energy consumption in silicon-based integrated circuits. A promising solution is to replace electrical wires with optical connections, for which a key component is a nanolaser that coherently emits into silicon-based waveguides to route information across a chip, in place of bulky off-chip devices. We report room temperature, sub- μm^2 footprint, quantum-well-in-nanopillar lasers grown directly on silicon and silicon-on-insulator (SOI) substrates that emit within the silicon-transparent wavelength range under optical excitation. The laser wavelength is controlled by changing the InGaAs quantum well thickness and alloy composition, quite independent of lattice mismatch with the InP barrier, a unique property of the 3D core-shell growth mode. We achieve excellent luminescence yield and low continuous wave transparency power due to the well-passivated InGaAs/InP interfaces. These sub- μm^2 footprint long-wavelength lasers could enable optoelectronic integration and photon routing with silicon waveguides on the technologically relevant SOI platform. © 2017 Optical Society of America

OCIS codes: (250.5960) Semiconductor lasers; (230.5590) Quantum-well, -wire and -dot devices; (310.6628) Subwavelength structures, nanostructures; (250.7270) Vertical emitting lasers; (230.3120) Integrated optics devices.

<https://doi.org/10.1364/OPTICA.4.000717>

1. INTRODUCTION

Optical interconnections at short length scales, on and between microprocessor chips, have tremendous prospects to scale communication bandwidth density and reduce energy consumption for next-generation silicon integrated circuits [1,2]. An intimate integration of active optoelectronic devices, including lasers, modulators, and photodetectors, with silicon photonic waveguides is important to best leverage the scalable manufacturing capabilities of silicon and reduce energy consumption. Indium-phosphide (InP)-based compound semiconductors are an ideal material choice for active photonic devices because they facilitate direct-bandgap quantum wells for the efficient emission and absorption of light in the silicon-transparent 1.15–1.5 μm wavelength range, which has minimal absorptive propagation loss in silicon waveguides.

However, direct epitaxial growth of InP-based compounds on silicon has proven to be extremely challenging due to mismatches in lattice constant and thermal expansion coefficients with silicon, leading to defects that are detrimental to device performance. Further, the temperature for InP epitaxial growth is very high (typically $>650^\circ\text{C}$), making it incompatible with CMOS post-processing requirements [3–5]. One of the proposed solutions is

to wafer bond group III-V lasers onto a silicon substrate, with evanescent coupling of light between the III-V gain medium and silicon-based cavity as the most popular approach thus far [6–8]. However, typical integration approaches implement edge-emitting laser structures, which have a very large footprint (hundreds of square micrometers to form a Fabry–Perot cavity). Such sizes are orders of magnitude too large to be viable for integration with electronic integrated circuits or silicon photonics. In addition, proportional to the active volume of the lasers, the power consumption of such devices is also extremely high, many orders of magnitude higher than that required for on-chip optical interconnects.

Recently, III-V compound semiconductor nanowires with footprints on the order of tens of nanometers have been shown to grow directly on silicon at low temperatures with excellent crystalline quality [9]. Work has also been reported on broad-area edge-emitting lasers using an ensemble nanowire-based active region [10,11]. However, a single as-grown nanowire laser would be highly desirable for high density, low power consumption applications [12]. Unfortunately, the nanowire lateral dimension is too small for good optical confinement. Additionally, most single nanowire lasers are demonstrated after removing from the growth

substrate [13–22], and the only as-grown nanowire laser emits at 825 nm [23]. These are not suitable for monolithic integration with silicon photonics.

We have recently reported a novel core-shell growth mode that results in single crystalline Wurtzite phase III-V nanopillars directly on a silicon substrate by catalyst-free metal-organic chemical vapor deposition [24,25]. Due to the 3D core-shell growth, nanopillars can scale up to several microns in height, while maintaining sub-micron diameter footprint with pristine crystalline quality in the bulk [26]. One major advantage of this core-shell structure is the minimal exposed surface of the active region, leading to brighter luminescence and lower dark current in devices. Using this growth mode, we reported the first demonstration of an InGaAs/GaAs nanolaser monolithically grown on silicon [27] and nanopillar lasers grown on transistors without compromising MOSFET electronic performance. This provides direct proof of the CMOS-compatibility of the low temperature growth mode [28]. In addition, we demonstrated InGaAs/GaAs nanopillar light emitting diodes (LED) directly modulated at 2.5 Gb/s and photodetectors at 1 Gb/s, all as-grown on a silicon substrate. With these devices, we demonstrated the first photonic link using as-grown nanopillar devices on a silicon substrate [29]. However, all these results are based on InGaAs nanopillars with lasing wavelengths around 900 nm. Most recently, we investigated InP-based nanopillar growth using the same growth mode to eventually achieve longer wavelengths. We demonstrated a compact InP bipolar junction phototransistor with a simultaneously high current gain (53.6), bandwidth (7 GHz), and responsivity (9.5 A/W) using a single crystalline InP nanopillar directly grown on a silicon substrate [30].

In this work, we report the first quantum-well (QW)-in-nanopillar laser as-grown on a silicon and silicon-on-insulator (SOI) substrate with silicon-transparent emission and a sub-micron footprint, by directly synthesizing high quality InP/InGaAs/InP QWs in nanopillars on silicon. We demonstrate a novel resonator with a silicon undercut-post structure to improve the optical quality factor. Further, we demonstrate the capability to tailor lasing wavelengths by changing the indium composition and thickness in InGaAs/InP QWs during growth, with emission ranging from 1.15 up to 1.3 μm , in spite of lattice mismatch between QW and InP barrier.

2. QUANTUM-WELL-IN-NANOPILLAR GROWTH

The $\text{In}_x\text{Ga}_{1-x}\text{As}$ ($x \sim 0.53$) material system is ubiquitous as the active region for lasers at telecommunication wavelengths. Such an active region typically consists of InGaAs/InAlGaAs QW grown lattice-matched or with a small strain on a (100)-InP substrate with a Zinc-Blende crystalline phase. We previously reported very efficient elastic stress relaxation at the GaAs/ $\text{In}_{0.2}\text{Ga}_{0.8}\text{As}$ interface due to the core-shell geometry and small diameter, resulting in a drastic increase of critical thickness as compared to the thin film case [31]. However, it was unclear that multiple lattice-mismatched layers can be grown on such pillars subsequently. In particular, it was not clear if a single or multiple $\text{In}_x\text{Ga}_{1-x}\text{As}$ /InP QW region can be grown on these Wurtzite-phase nanopillars with the side walls having an undetermined crystalline facet. Here, we demonstrate such growth with excellent optical quality for the first time.

First, the InP nanopillars are grown on a Si (111) substrate. Subsequently, a series of samples with varied numbers of InGaAs/InP QWs were grown onto the InP core in a core-shell

manner by controlling organometallic precursor flows. A final 100 nm InP layer is grown as the surface passivation layer, thus cladding the interfaces of the active region. Figure 1(a) shows the 85° tilt-view scanning electron microscopy (SEM) image of spontaneously nucleated nanopillars grown on a silicon substrate. The nanopillars align to the four degenerate (111) directions of the silicon substrate, further evidence of monolithic crystalline growth. Note that the silicon substrate surface is clean and free of polycrystalline thin film deposition, in sharp contrast to those with InGaAs/GaAs nanopillars [26–32]. This clean silicon

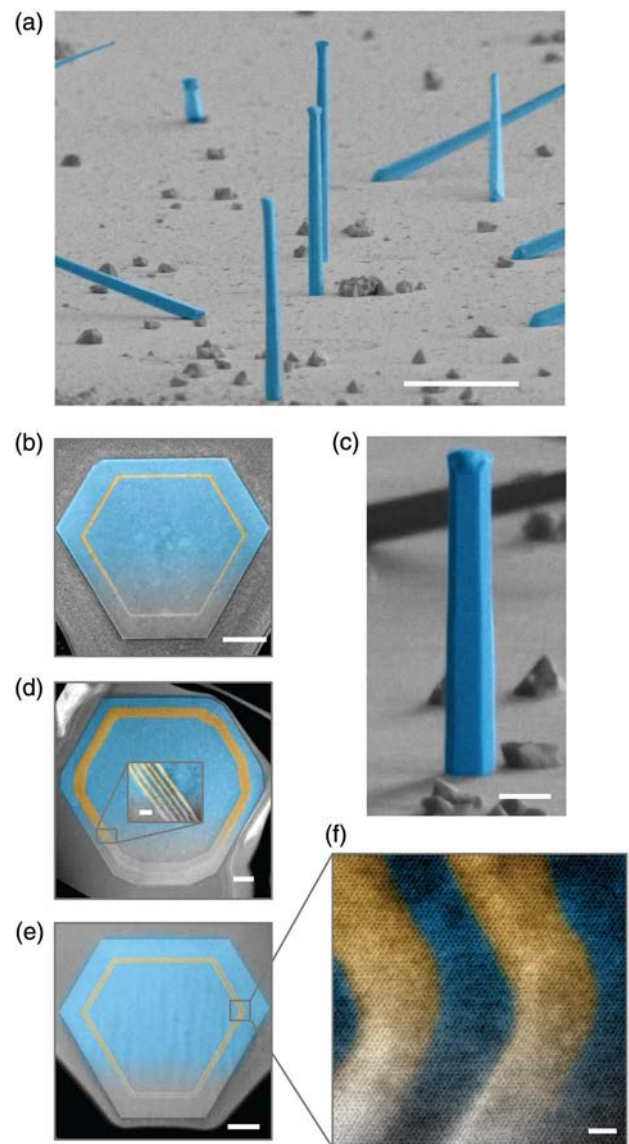


Fig. 1. (a) Scanning electron micrograph of spontaneously nucleated InP nanopillars growing directly on (111) silicon, with the growth axis aligned along degenerate (111) directions. Note that the silicon substrate surface is clean and free of polycrystalline thin film deposition, unlike those with InGaAs/GaAs nanopillars [26–32]. (b) Cross-sectional TEM image of a single QW (highlighted in yellow). (c) Close-up SEM of an exemplary single nanopillar. (d) Cross-sectional TEM of a nanopillar with five QWs grown conformally on the InP core, with an inset showing the individual QWs. (e) Cross-sectional TEM of a nanopillar with two QWs, and (f) high resolution TEM image showing the continuity of the lattice. Scale bars: (a) 5 μm , (b) 100 nm, (c) 1 μm , (d) 100 nm (inset: 20 nm), (e) 100 nm, and (f) 2 nm.

substrate facilitates simple silicon etch processing to be performed after growth of the nanopillars, as described in the section on the undercut cavity laser. The QWs inside the nanopillar are visualized using cross-sectional transmission electron microscopy (TEM). Figures 1(b), 1(d), and 1(e) show the cross-sectional TEM images of a nanopillar with one, five, and two QWs inside, respectively. Due to an atomic mass difference, the InGaAs QW can be distinguished from InP as a brighter hexagonal ring. The thickness of the QW is measured to be ~ 5 nm. The interface between InP and InGaAs is sharp and free of any defects or dislocations, attesting to the superior quality of the active region.

Figure 1(c) shows an exemplary nanopillar, with a typical diameter of ~ 800 nm and a height of $6\text{--}7$ μm . Multiple QWs are desirable to provide sufficient gain for lasing. It is interesting to note in Fig. 1(d) that the multiple QWs show up as hexagonal rings conformal to the core-shell growth. Figure 1(f) is a high resolution TEM image inset of the two QW cross sections. Seamless continuity of the Wurtzite crystal lattice through the heterostructure can be observed, with image contrast from the different atomic masses.

3. LUMINESCENCE YIELD AND TRANSPARENCY

Excellent optical quality of the QW is attested by photoluminescence measurements on as-grown InP/InGaAs/InP nanopillars. A calibrated absolute luminescence measurement can be used to measure the Fermi level split of the electrons and holes ΔF , since the spontaneous emission count rate r_{sp} (photons/s/cm²/eV) depend exponentially on the difference of ΔF and the photon energy $\hbar\omega$. This is a new extension of the widely adapted “contactless I-V” technique used in the characterization of solar cells [33–36]. Absolute counts can be determined using a calibration with known reflective properties. In this case, the calibration was performed using a 1550 nm laser reflected off a Lambertian reflecting surface (Spectralon). Using an absolute measurement of the laser power, the counts measured on the spectrometer can be converted into photons, and the Fermi level split is determined as

$$\Delta F - \hbar\omega = k_B T \ln\left(\frac{r_{sp}}{r_0}\right), \quad (1)$$

where r_0 depends on fundamental constants and the emissivity of the luminescing layer (Supplement 1 section I). This technique is valuable in gauging the excitation intensity at which the QW active material starts to show optical gain. More precisely, this helps us determine the current density at which the Fermi level split equals the bandgap, known as the transparency current density. Typically, good quality QW heterostructures have a transparency current density of $50\text{--}100$ A/cm² per QW layer [37]. To determine this metric using photoluminescence, the nanopillar is excited with a continuous wave 660 nm (1.88 eV) laser that is absorbed efficiently by the InP cladding layer. An individual InP nanopillar is measured at 5 K and 293 K. The InP/InGaAs/InP nanopillar case is the same. Since the InP nanopillars have a very low surface recombination velocity, as reported in Ref. [32], the carriers generated in the InP cladding are efficiently captured by the QW. This enables us to achieve a very high carrier concentration in the QW, resulting in a low continuous wave room temperature transparency pump power density for the QW. Figure 2(a) shows a schematic of the process, with low excitation PL spectra of a single QW nanopillar in Fig. 2(b). As observed in Fig. 2(b), the emission from the QW is orders of magnitude

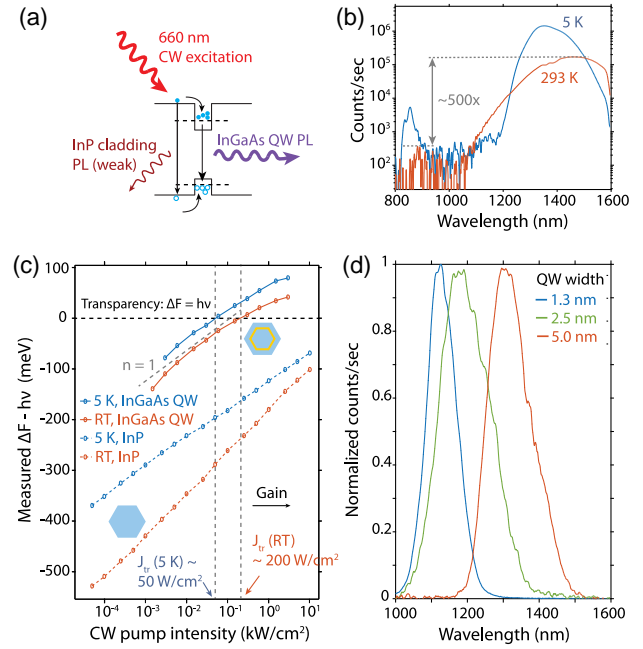


Fig. 2. QW luminescence and transparency conditions. (a) Schematic showing indirect excitation of QWs using 660 nm light, which is absorbed in the InP cladding layer, followed by rapid electron-hole capture into the QW heterostructure. This results in a carrier concentrating effect, leading to a high steady state carrier density at low pump excitation power. (b) Photoluminescence (PL) spectra for indirect excitation of a single QW embedded in an InP nanopillar, showing enhanced luminescence in the heterostructure compared to the bulk. This effect is more pronounced at room temperature, as explained in the text. (c) An absolute measurement of the luminescence allows us to extract the chemical potential of the photons, which exactly equals the steady state Fermi level split of the electrons and holes—thus reflecting the carrier concentration. This is plotted in (c) for the case of a QW heterostructure and compared with an undoped InP nanopillar, revealing a much higher Fermi level split in excess of the bandgap in the QW case compared to bulk InP. Additionally, in the QW case, the room temperature luminescence is less diminished compared to low temperature, reflecting a higher internal luminescence yield due to the beneficial effect of core-shell surface passivation. (d) Pillars with different growth times for the QW layer show PL spectra reflecting a quantum size effect, leading to wavelength tunability over 200 nm in the silicon-transparent window.

higher than that from the InP barrier layer, a clear indication of efficient carrier collection. This effect is even more significant at room temperature due to the surface passivation effect from the high bandgap cladding layer, which preserves the heterostructure emission even at higher temperatures.

The excitation dependence is plotted in Fig. 2(c) at 5 K and room temperature. The Y-axis shows the difference from transparency $\Delta F - \hbar\omega$ in meV using Eq. (1). First, we calculate the internal luminescence yield from the ratio of room temperature to low temperature counts. We find that the internal yield is as high as 25% and stays fairly constant, even at low pump powers. This can be fit to a carrier recombination model, with the dominant non-radiative recombination path being Shockley–Read–Hall recombination at the InP/InGaAs interface with an extremely low interfacial recombination velocity of ~ 10 cm/s (Supplement 1 section II). This internal luminescence yield is two orders of magnitude higher than that for undoped InP

nanopillars, which is measured to be 0.3% and increases with pump intensity due to the saturation of non-radiative centers at the naked InP surface (dashed curves). In addition, the luminescence yield is on par with that of a commercial planar InGaAs QW epitaxially grown on a lattice-matched InP substrate, measured to be 30%–33% using the same technique.

We point out that the transparency condition is easily achieved for QW at a pump excitation power of 200 W/cm^2 at room temperature. Even if one assumes that 100% of the incident pump power on the nanopillar cross section is absorbed, this corresponds to an equivalent electrical pump current density of $\sim 110 \text{ A/cm}^2$ for the 660 nm (1.88 eV) photons. To the best of our knowledge, this is the first time this metric has been measured for nanowire or nanopillar-based gain media and is on par with reported values for traditional III-V thin film QWs [37]. The low transparency power is very promising for energy efficient nanopillar-based light sources on chip.

A verification of the physical dimension of the QW is obtained from the quantum size effect. The quantization energy will increase as the thickness of QW reduces, leading to a shorter wavelength emission. The PL measurement results in Fig. 2(d) show that as QW thickness reduces from 5 to 1.3 nm, the wavelength blue-shifts by approximately 200 nm. This is consistent with a finite barrier QW analysis for $\text{In}_{0.45}\text{Ga}_{0.55}\text{As}$, which has a 0.55% lattice constant mismatch with the InP nanopillar core. In spite of this, we have been able to grow multiple QW at this alloy concentration, with total thickness two to three times the thin film critical thickness for this lattice mismatch (further details in Supplement 1 Section V).

4. AS-GROWN QW-NANOLASERS ON SOI

InGaAs nanopillars grown directly on silicon are able to sustain significant optical feedback via helically propagating modes, in spite of the small refractive index difference with the silicon substrate [27]. In that case, the pillar has a slightly higher refractive index compared to the substrate. Hence, a mode propagating at a grazing angle to the substrate interface can still experience total internal reflection. However, in the InP case, the refractive index of the silicon substrate is higher, thus making it challenging to achieve optical feedback at the substrate interface. One approach is to grow the nanopillars onto a silicon on insulator (SOI) substrate, where the Si-SiO₂ layers enhance the bottom reflection of the nanopillar cavity mode due to the low index of the oxide. In the SOI substrate, the buried silicon dioxide layer is $\sim 2 \mu\text{m}$ thick, whereas the silicon layer is as thin as $\sim 500 \text{ nm}$, so that reflected light at the Si-SiO₂ interface can be efficiently collected back to the nanopillar cavity and contribute to cavity feedback. An advantage of this approach is that the strongly confined fundamental transverse order mode can experience sufficient optical feedback for lasing.

Figure 3(a) illustrates the as-grown nanopillar configuration. Under a pulsed optical pump directly exciting the QW at 5 K, lasing is successfully obtained on the as-grown nanopillars on SOI. The lasing spectra for different growth runs with indium composition tuning are shown in Fig. 3(b). With increasing indium composition, the PL and lasing wavelength can be shifted from ~ 1200 to $\sim 1300 \text{ nm}$, clearly illustrating that the growth is not constrained by lattice matching between InGaAs QW and InP barrier [31]. This is extremely promising for wavelength

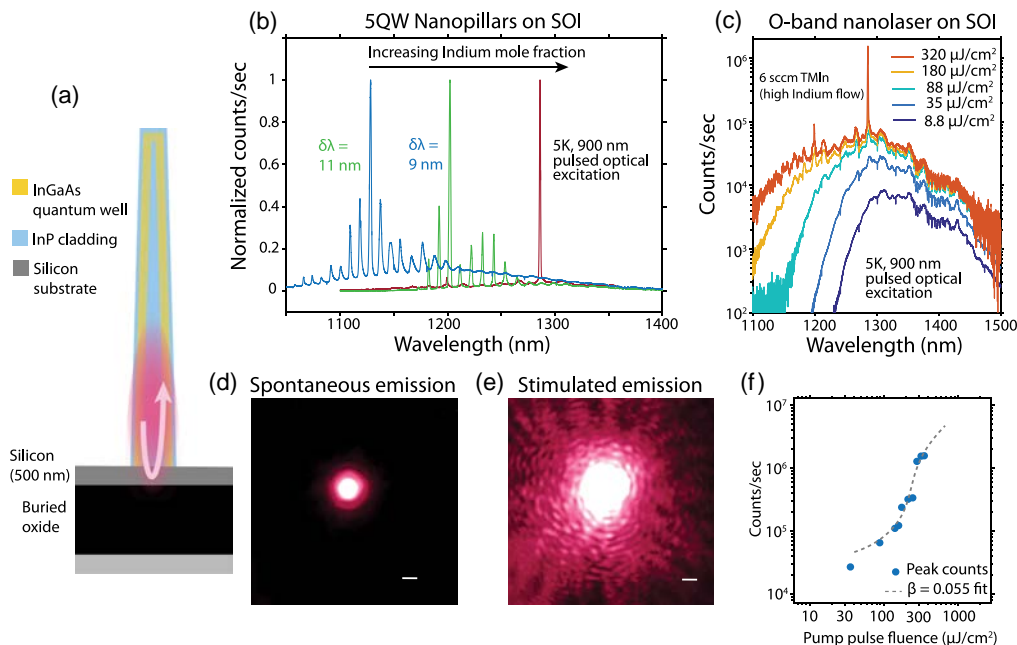


Fig. 3. As-grown nanopillar lasers on a SOI substrate. (a) Nanopillar lasers have been monolithically integrated on a SOI substrate, which is relevant for silicon photonics. The silicon layer is 500 nm thick. The low thickness enhances the reflection from the bottom facet of the pillar, leading to multiple longitudinal mode lasing with Fabry–Perot mode separation consistent with the pillar length. (b) Tuning the indium composition of the QW can be used to shift the lasing oscillation red from ~ 1100 to $\sim 1300 \text{ nm}$, indicating a path toward the 1310 nm range that is interesting for on-chip photon routing. The lower set of spectra shows spontaneous emission, with the upper set showing spectra above the lasing threshold on the same pillars. (c) Single mode lasing at 1286 nm (within the O-band) has been obtained by tuning to a higher indium composition during growth. (d) and (e) Near-field images also show lasing mode profiles, with an incoherent image for the PL below threshold, followed by a spatially coherent speckle pattern after the onset of lasing. (f) The measured L–L curve for the laser in (c) shows a characteristic kink at threshold.

design for silicon transparency. The Fabry–Perot mode spacing is typically 10 nm, consistent with an effective cavity length of 10–20 μm for the nanopillars. Figure 3(c) shows the emission spectra of a 1300-nm nanopillar laser (QW grown with higher TMIn flow of 6 sccm) under various pumping levels. It is clear that the spontaneous emission is clamped at the lasing threshold, and a single longitudinal mode laser emission at 1286 nm is obtained. The near-field images below and above threshold are shown in Figs. 3(d) and 3(e), respectively. The latter clearly shows a coherent speckle pattern above the lasing threshold. Figure 3(f) shows the L–L curve corresponding to the laser in Fig. 3(c) with a typical lasing threshold behavior.

5. UNDERCUT CAVITY QW-NANOLASER

An alternative and novel approach to increase the nanopillar/Si interface reflection is to create an abrupt structural discontinuity at the interface, shown in Fig. 4(a). The nanopillar is supported by a silicon post having a smaller diameter than the nanopillar and created by a selective undercut etching process of the silicon substrate. Figure 4(a) shows an 85° tilt-view SEM image of a nanopillar supported by an undercut silicon post, where the nanopillar is highlighted in blue. As observed in the zoom-in SEM image, the InP nanopillar remains intact after the Si etching. The exposed silicon substrate can be etched using this method because of the absence of any polycrystalline III-V thin film. The small air gap at the nanopillar base provides enhanced reflection for the helically propagating nanopillar modes. Figure 4(b) shows the

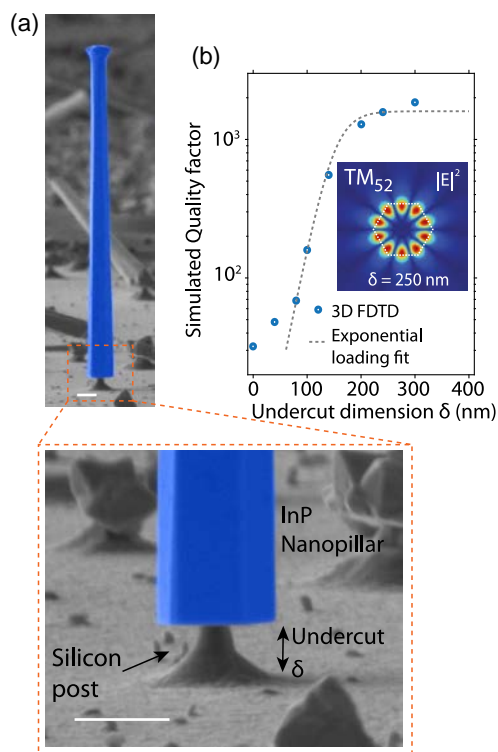


Fig. 4. Undercut cavity structure. (a) SEM image of nanopillar with a selective silicon undercut etch using $\text{SF}_6 + \text{O}_2$ plasma. The etch leaves the InP pillar unaffected, while isotropically etching a pedestal under the pillar in a self-aligned manner. The undercut is 1 μm . (b) This enhances the quality factor of modes, with an exemplary TM_{52} mode revealing high quality factor greater than 10^3 with a small undercut etch δ of 150–200 nm. Both scale bars: 1 μm .

optical cavity quality factor Q calculated using 3D finite difference time domain simulations for different undercut dimensions δ in the silicon structure. As the undercut δ increases above 200 nm, Q is simulated to exceed 1000, and it is no longer limited by proximity to the silicon. The inset of Fig. 4(b) shows that the simulated cross-sectional field distribution is a symmetric high order mode with intensity peaks close to the edge of the nanopillar.

By incorporating five InGaAs QWs into this novel high- Q undercut cavity, long-wavelength nanopillar lasers are achieved under pulsed optical pumping from 5 K up to room temperature. Figure 5(a) shows the PL spectra above and below the threshold, with the lasing wavelength at 1220–1230 nm and some dependence of the lasing peak on temperature. The lasing peak power is plotted as a function of the pump pulse fluence in Fig. 5(b) for various temperatures. A typical S-shape near the threshold is observed. These L–L curves can be fit with a rate equation model and spontaneous emission coupling factor β of 1%–5%, which is typical for such compact laser cavities. An important outcome of the low dimensional heterostructure is the reduced temperature sensitivity of the lasing threshold as predicted by Arakawa and Sakaki [38]. From 5 K to 300 K, the threshold pump fluence increases from ~ 20 to 200 $\mu\text{J}/\text{cm}^2$. This corresponds to a laser characteristic temperature, T_0 , of 128 K. This T_0 value is surprisingly high compared to typical InGaAs QW edge-emitting lasers on a lattice-matched InP substrate, despite the small footprint on the Si substrate acting as a heat sink. In Supplement 1 Section IV, we describe measurements to ascertain the thermal resistance of a single nanopillar device. The robust temperature performance attests to the superior quality of the nanopillar QW gain material.

The same nanopillar was also measured under continuous wave pump. Figure 5(c) shows the PL spectra at low temperature with direct excitation of the QW with a 980 nm CW pump. At low pump power of 5 W/cm^2 , the PL spectrum shows narrow modes with 1.6 nm linewidth. The onset of continuous wave

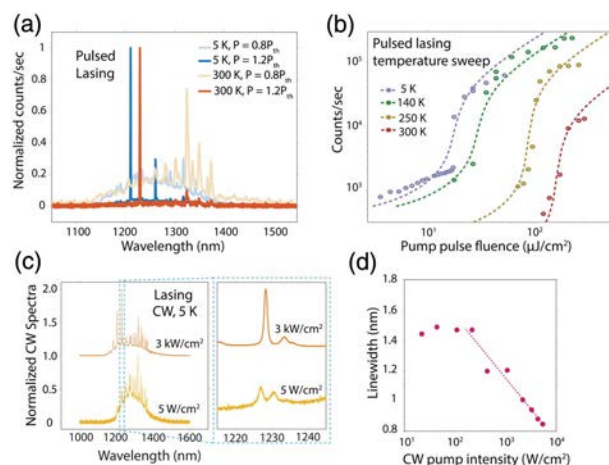


Fig. 5. Undercut cavity lasing up to RT. (a) Pulsed optical excitation leads to lasing from 5 K up to room temperature, showing an order of magnitude side mode suppression. (b) The lasing L–L curves show a characteristic S-shape all the way to room temperature and can be fit with a rate equation model. The threshold pump fluence shows reduced temperature sensitivity compared to reports for bulk gain media in nanopillars and nanowires. (c) Low temperature (5 K), continuous wave luminescence spectra linewidth narrowing (d) to ~ 0.8 nm at the onset of lasing.

lasing is indicated by linewidth collapse to 0.8 nm when the pump power is increased to 3 kW/cm². To the best of our knowledge, this is the first report of continuous wave lasing from nanopillar or nanowire-based structures at a silicon-transparent wavelength.

6. DISCUSSION

In summary, we report two long-wavelength QW-in-nanopillar laser configurations, both monolithically grown on silicon with a subwavelength footprint. The InGaAs QW active gain material is obtained for the first time on InP nanopillars with various indium composition and thickness to tailor emission wavelength. The optical material quality was verified to be on par with III-V epitaxial QWs, using the transparency power density and luminescence yield as metrics. Due to the unique 3D core-shell growth mode, the nanopillar can scale in diameter up to micrometer size, leading to sufficient optical confinement and modal gain at long wavelengths. We demonstrated two different methods to monolithically fabricate optical resonators on silicon-based platforms. A selective silicon etch has been used to define an undercut nanopillar cavity with a quality factor higher than 10³, while maintaining subwavelength footprint. This undercut cavity laser operates up to room temperature and displays a high laser characteristic temperature T_0 of 128 K. By growing nanopillars on an SOI substrate, a vertical Fabry–Perot cavity is created with enhanced reflection from the Si-SiO₂ interface of the SOI substrate. As-grown nanolasers were therefore achieved on SOI at wavelengths ranging from 1.15 to 1.3 μm—suitable for routing via silicon waveguides. We would like to emphasize that the nanopillar lasers have a footprint of one micron or less. We believe our result is an important step toward integrating laser sources on silicon for optical interconnect applications. Related work [39] has been published after this paper was submitted.

Funding. National Science Foundation (NSF) (0939514, 1335609); National Research Foundation Singapore (NRF) (NRF-CRP14-2014-03); Tsinghua-Berkeley Shenzhen Institute.

Acknowledgment. We thank Dr. Hai-Feng Liu and Dr. Edris M. Mohammed from Intel Corporation for valuable discussions. We acknowledge the support of the National Center for Electron Microscopy, LBNL. We also thank Dr. Saniya Deshpande and Dr. Daria Skuridina for assistance with crystal growth and Zibo Gong for help with FDTD simulations.

[†]These authors contributed equally to this work.

See [Supplement 1](#) for supporting content.

REFERENCES

1. A. V. Krishnamoorthy, "Computer systems based on silicon photonic interconnects," *Proc. IEEE* **97**, 1337–1361 (2009).
2. D. A. B. Miller, "Device requirements for optical interconnects to silicon chips," *Proc. IEEE* **97**, 1166–1185 (2009).
3. H. Liu, "Long-wavelength InAs/GaAs quantum-dot laser diode monolithically grown on Ge substrate," *Nat. Photonics* **5**, 416–419 (2011).
4. T. Wang, H. Liu, A. Lee, F. Pozzi, and A. Seeds, "1.3-μm InAs/GaAs quantum-dot lasers monolithically grown on Si substrates," *Opt. Express* **19**, 11381–11386 (2011).
5. Y. Wan, Q. Li, A. Y. Liu, A. C. Gossard, J. E. Bowers, E. L. Hu, and K. M. Lau, "Optically pumped 1.3 μm room-temperature InAs quantum-dot micro-disk lasers directly grown on (001) silicon," *Opt. Lett.* **41**, 1664–1667 (2016).
6. A. W. Fang, H. Park, O. Cohen, R. Jones, M. J. Paniccia, and J. E. Bowers, "Electrically pumped hybrid AlGaInAs-silicon evanescent laser," *Opt. Express* **14**, 9203–9210 (2006).
7. J. Van Campenhout, P. Rojo-Romeo, P. Regreny, C. Seassal, D. Van Thourhout, S. Verstuyft, L. Di Coccio, J.-M. Fedeli, C. Lagahe, and R. Baets, "Electrically pumped InP-based microdisk lasers integrated with a nanophotonic silicon-on-insulator waveguide circuit," *Opt. Express* **15**, 6744–6749 (2007).
8. Y. H. Lo, R. Bhat, D. M. Hwang, C. Chua, and C.-H. Lin, "Semiconductor lasers on Si substrates using the technology of bonding by atomic rearrangement," *Appl. Phys. Lett.* **62**, 1038–1040 (1993).
9. L. C. Chuang, M. Moewe, C. Chase, N. P. Kobayashi, and C. Chang-Hasnain, "Critical diameter for III-V nanowires grown on lattice-mismatched substrates," *Appl. Phys. Lett.* **90**, 043115 (2007).
10. T. Frost, A. Banerjee, K. Sun, S. L. Chuang, and P. Bhattacharya, "InGaN/GaN quantum dot ($\lambda = 630$ nm) laser," *IEEE J. Quantum Electron.* **49**, 923–931 (2013).
11. A. Hazari, A. Aiello, T. Ng, B. S. Ooi, and P. Bhattacharya, "III-nitride disk-in-nanowire 1.2 μm monolithic diode laser on (001)silicon," *Appl. Phys. Lett.* **107**, 191107 (2015).
12. R. Yan, D. Gargas, and P. Yang, "Nanowire photonics," *Nat. Photonics* **3**, 569–576 (2009).
13. A. H. Chin, S. Vaddiraju, A. V. Maslov, C. Z. Ning, M. K. Sunkara, and M. Meyyappan, "Near-infrared semiconductor subwavelength-wire lasers," *Appl. Phys. Lett.* **88**, 163115 (2006).
14. J. C. Johnson, "Single gallium nitride nanowire lasers," *Nat. Mater.* **1**, 106–110 (2002).
15. R. Agarwal, C. J. Barrelet, and C. M. Lieber, "Lasing in single cadmium sulfide nanowire optical cavities," *Nano Lett.* **5**, 917–920 (2005).
16. F. Qian, Y. Li, S. Gradecak, H.-G. Park, Y. Dong, Y. Ding, Z. L. Wang, and C. M. Lieber, "Multi-quantum-well nanowire heterostructures for wavelength-controlled lasers," *Nat. Mater.* **7**, 701–706 (2008).
17. Y. Xiao, C. Meng, P. Wang, Y. Ye, H. Yu, S. Wang, F. Gu, L. Dai, and L. Tong, "Single-nanowire single-mode laser," *Nano Lett.* **11**, 1122–1126 (2011).
18. A. Pan, W. Zhou, E. S. P. Leong, R. Liu, A. H. Chin, B. Zou, and C. Z. Ning, "Continuous alloy-composition spatial grading and superbroad wavelength-tunable nanowire lasers on a single chip," *Nano Lett.* **9**, 784–788 (2009).
19. M. A. Zimmler, J. Bao, F. Capasso, S. Mueller, and C. Ronning, "Laser action in nanowires: observation of the transition from amplified spontaneous emission to laser oscillation," *Appl. Phys. Lett.* **93**, 051101 (2008).
20. S. Chu, G. Wang, W. Zhou, Y. Lin, L. Chernyak, J. Zhao, J. Kong, L. Li, J. Ren, and J. Liu, "Electrically pumped waveguide lasing from ZnO nanowires," *Nat. Nanotechnol.* **6**, 506–510 (2011).
21. B. Hua, J. Motohisa, Y. Kobayashi, S. Hara, and T. Fukui, "Single GaAs/GaAs core-shell nanowire lasers," *Nano Lett.* **9**, 112–116 (2009).
22. D. Saxena, S. Mokkaapati, P. Parkinson, N. Jiang, Q. Gao, H. H. Tan, and C. Jagadish, "Optically pumped room-temperature GaAs nanowire lasers," *Nat. Photonics* **7**, 963–968 (2013).
23. B. Mayer, L. Janker, B. Loitsch, J. Treu, T. Kostenbader, S. Lichtmannecker, T. Reichert, S. Morkoetter, M. Kaniber, G. Abstreiter, C. Gies, G. Koblmueeller, and J. J. Finley, "Monolithically integrated high-β nanowire lasers on silicon," *Nano Lett.* **16**, 152–156 (2016).
24. M. Moewe, L. C. Chuang, S. Crankshaw, C. Chase, and C. Chang-Hasnain, "Atomically sharp catalyst-free wurtzite GaAs/AlGaAs nanoneedles grown on silicon," *Appl. Phys. Lett.* **93**, 023116 (2008).
25. F. Ren, K. W. Ng, K. Li, H. Sun, and C. J. Chang-Hasnain, "High-quality InP nanoneedles grown on silicon," *Appl. Phys. Lett.* **102**, 012115 (2013).
26. K. W. Ng, W. S. Ko, T.-T. D. Tran, R. Chen, M. V. Nazarenko, F. Lu, V. G. Dubrovskii, M. Kamp, A. Forchel, and C. J. Chang-Hasnain, "Unconventional growth mechanism for monolithic integration of III-V on silicon," *ACS Nano* **7**, 100–107 (2013).
27. R. Chen, T.-T. D. Tran, K. W. Ng, W. S. Ko, L. C. Chuang, F. G. Sedgwick, and C. Chang-Hasnain, "Nanolasers grown on silicon," *Nat. Photonics* **5**, 170–175 (2011).
28. F. Lu, T.-T. D. Tran, W. S. Ko, K. W. Ng, R. Chen, and C. Chang-Hasnain, "Nanolasers grown on silicon-based MOSFETs," *Opt. Express* **20**, 12171–12176 (2012).

29. R. Chen, K. W. Ng, W. S. Ko, D. Parekh, F. Lu, T.-T. D. Tran, K. Li, and C. Chang-Hasnain, "Nanophotonic integrated circuits from nanoresonators grown on silicon," *Nat. Commun.* **5**, 4325 (2014).
30. W. S. Ko, I. Bhattacharya, T.-T. D. Tran, K. W. Ng, S. A. Gerke, and C. Chang-Hasnain, "Ultra-high responsivity-bandwidth product in a compact InP nanopillar phototransistor directly grown on silicon," *Sci. Rep.* **6**, 33368 (2016).
31. M. V. Nazarenko, N. V. Sibirev, K. W. Ng, F. Ren, W. S. Ko, V. G. Dubrovskii, and C. Chang-Hasnain, "Elastic energy relaxation and critical thickness for plastic deformation in the core-shell InGaAs/GaAs nanopillars," *J. Appl. Phys.* **113**, 104311 (2013).
32. K. Li, K. W. Ng, T.-T. D. Tran, H. Sun, F. Lu, and C. Chang-Hasnain, "Wurtzite-phased InP micropillars grown on silicon with low surface recombination velocity," *Nano Lett.* **15**, 7189–7198 (2015).
33. P. Wuerfel, "The chemical potential of radiation," *J. Phys. C* **15**, 3967–3985 (1982).
34. T.-T. D. Tran, H. Sun, K. W. Ng, F. Ren, K. Li, F. Lu, E. Yablonovitch, and C. Chang-Hasnain, "High brightness InP micropillars grown on silicon with Fermi level splitting larger than 1 eV," *Nano Lett.* **14**, 3235–3240 (2014).
35. A. Delamarre, L. Lombez, and J. Guillemoles, "Contactless mapping of saturation currents of solar cells by photoluminescence," *Appl. Phys. Lett.* **100**, 131108 (2012).
36. T. Trupke, R. A. Bardos, M. C. Schubert, and W. Warta, "Photoluminescence imaging of silicon wafers," *Appl. Phys. Lett.* **89**, 044107 (2006).
37. M. Rosenzweig, M. Moehle, H. Dueser, and H. Venghaus, "Threshold-current analysis of InGaAs-InGaAsP multi-quantum well separate-confinement lasers," *IEEE J. Quantum Electron.* **27**, 1804–1811 (1991).
38. Y. Arakawa and H. Sakaki, "Multidimensional quantum well laser and temperature dependence of its threshold current," *Appl. Phys. Lett.* **40**, 939–941 (1982).
39. F. Schuster, J. Kapraun, G. N. Malheiros-Silveira, S. Deshpande, and C. Chang-Hasnain, "Site-controlled growth of monolithic InGaAs/InP quantum well nanopillars on silicon," *Nano Lett.* **17**, 2697–2702 (2017).